

# **IISE Transactions**



ISSN: (Print) (Online) Journal homepage: <a href="https://www.tandfonline.com/loi/uiie21">https://www.tandfonline.com/loi/uiie21</a>

# Real-time detection of clustered events in videoimaging data with applications to additive manufacturing

Hao Yan, Marco Grasso, Kamran Paynabar & Bianca Maria Colosimo

To cite this article: Hao Yan, Marco Grasso, Kamran Paynabar & Bianca Maria Colosimo (2021): Real-time detection of clustered events in video-imaging data with applications to additive manufacturing, IISE Transactions, DOI: <u>10.1080/24725854.2021.1882013</u>

To link to this article: <a href="https://doi.org/10.1080/24725854.2021.1882013">https://doi.org/10.1080/24725854.2021.1882013</a>

+	View supplementary material 🗹
	Published online: 18 Mar 2021.
	Submit your article to this journal 🗷
ılıl	Article views: 272
Q <sup>N</sup>	View related articles 🗹
CrossMark	View Crossmark data 🗗





# Real-time detection of clustered events in video-imaging data with applications to additive manufacturing

Hao Yan<sup>a</sup> , Marco Grasso<sup>b</sup> , Kamran Paynabar<sup>c</sup>, and Bianca Maria Colosimo<sup>b</sup>

<sup>a</sup>School of Computing, Informatics, and Decision Systems Engineering, Arizona State University, Tempe, AZ, USA; <sup>b</sup>Dipartimento di Meccanica, Politecnico di Milano, Italy; <sup>c</sup>H. Milton Stewart School of Industrial and Systems Engineering, Georgia Institute of Technology, Atlanta, GA, USA

#### **ABSTRACT**

The use of video-imaging data for in-line process monitoring applications has become popular in industry. In this framework, spatio-temporal statistical process monitoring methods are needed to capture the relevant information content and signal possible out-of-control states. Video-imaging data are characterized by a spatio-temporal variability structure that depends on the underlying phenomenon, and typical out-of-control patterns are related to events that are localized both in time and space. In this article, we propose an integrated spatio-temporal decomposition and regression approach for anomaly detection in video-imaging data. Out-of-control events are typically sparse, spatially clustered and temporally consistent. The goal is not only to detect the anomaly as quickly as possible ("when") but also to locate it in space ("where"). The proposed approach works by decomposing the original spatio-temporal data into random natural events, sparse spatially clustered and temporally consistent anomalous events, and random noise. Recursive estimation procedures for spatio-temporal regression are presented to enable the real-time implementation of the proposed methodology. Finally, a likelihood ratio test procedure is proposed to detect when and where the anomaly happens. The proposed approach was applied to the analysis of high-sped video-imaging data to detect and locate local hot-spots during a metal additive manufacturing process.

#### **ARTICLE HISTORY**

Received 2 March 2020 Accepted 21 December 2020

#### **KEYWORDS**

Spatio-temporal regression; video-imaging data; statistical process monitoring; in-situ defect detection; metal additive manufacturing; laser powder bed fusion

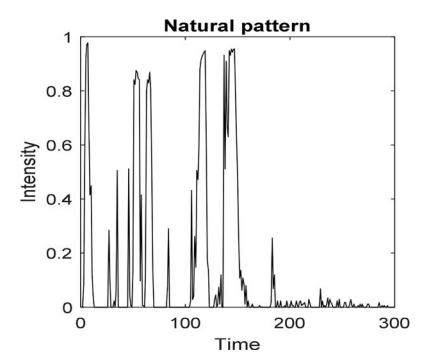
#### 1. Introduction

Nowadays, the use of spatio-temporal data streams, such as images and videos, in change detection and process monitoring is becoming more popular in advanced manufacturing systems (Megahed *et al.*, 2011; Megahed and Jones Farmer, 2015) and other complex systems. On the one hand, the increasing availability of compact, low-cost, and robust machine vision systems that can be easily integrated into production plants has enabled real-time image acquisition. On the other hand, continuously improving computational capabilities has made an in-line analysis of image streams more feasible. An effective anomaly detection method for such data streams should address the following challenges:

- 1. *High dimensionality*: High-resolution images are comprised of millions of pixels.
- High velocity: A standard video camera collects 24
  frames per second, whereas a high-speed camera may
  acquire thousands of frames per second, which requires
  a computationally efficient real-time analysis of
  image frames.

- No anomaly labels: In most industrial applications, there
  are few anomaly samples available and normally no
  labels are provided to assess whether the sample is
  anomalous or not.
- 4. Complex spatio-temporal correlation structure: Neighbor pixels are spatially correlated, and consecutive image frames are temporally correlated.
- 5. Measurement uncertainty: Measurement noise may mask relevant spatial and temporal patterns.

One specific goal addressed by this article is to detect spatio-temporally correlated anomalies by separating them from the natural foreground and background patterns captured in video-image data. To this aim, this study presents a new scalable spatio-temporal decomposition methodology to detect the structured anomalies in real-time. The method relies on the following common assumptions about the spatial and temporal structure of foreground natural events and anomaly events: (i) the foreground natural events are sparse and random in the spatio-temporal domain; and (ii) the anomaly event is sparse, spatially clustered and temporally consistent. It is worth noting that as long as these assumptions hold, the proposed methodology is applicable to any spatio-temporal process monitoring/change detection.



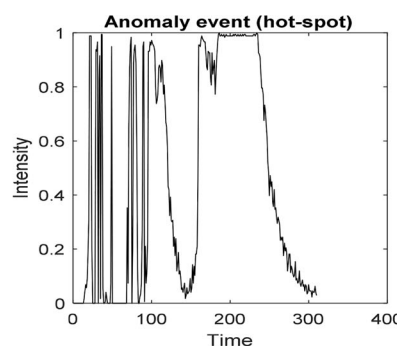


Figure 1. Spatial temporal structure of the video-frame. Spatial structure of the hot-spot is presented along with the LHZ and the spatters (left panel). Example of a natural temporal pattern of pixel intensities where peaks are caused by the quick transition of spatters or by the LHZ (middle panel); example of an out-of-control temporal pattern of pixel intensities in the presence of a hot-spot (right panel).

Furthermore, we propose an efficient and recursive estimation procedure to detect and locate the anomaly event in real-time, i.e., as soon as a new data point (e.g., a video frame) is recorded. In order to automatically signal the occurrence of an anomaly event, we propose to combine the penalized spatio-temporal regression framework with a Likelihood Ratio Test (LRT) for change detection, process monitoring, and anomaly localization (Mood, 1950; Gertler, 2017). Sub-section 1.1 presents a motivating case study used to demonstrate and test the effectiveness of the proposed methodology.

#### 1.1. A motivating case study

In the recent years, particular interest has been devoted to the use of machine vision in metal Additive Manufacturing (AM) applications (Everton et al., 2016; Grasso and Colosimo, 2017). Indeed, the layer-wise production paradigm involved in AM allows one to acquire images and videos during the production of each layer. This yields the capability of measuring several quantities that are proxies of the part quality and the process stability while the part is being produced, enabling several benefits including defect detection, waste reduction and cost savings in post-process inspection. In-situ and in-line monitoring of manufacturing processes based on video-imaging data require the capability of making sense of big data streams in an efficient and sound way.

The motivating case study considers dealing with in-situ defect detection in Laser Powder Bed Fusion (LPBF). LPBF is a metal AM approach where a laser beam is used to selectively melt a powder bed (Stucker et al., 2010). Despite the great industrial potential of LPBF technology, its actual application is limited by the various kinds of defects that may originate during the process (Everton et al., 2016; Grasso and Colosimo, 2017). Nowadays, most industrial LPBF systems are equipped with sensors suitable to measure several quantities during the process (Grasso and Colosimo, 2017), but what is still lacking is the availability of analytical tools able to quickly make sense of the gathered data during the process and automatically signal the onset of defects and process instabilities. In this framework, in-situ video imaging allows one to monitor the stability of the process while

the part is being produced on a layer-by-layer basis and to detect the onset of process defects. However, although such defects are visually detectable from image streams, automatic and real-time analysis of images is imperative for scalable and effective process monitoring. The main goal of the real case study is to automatically detect and locate over-heating phenomena in LPBF known as "hot-spots" via in-situ video-imaging. A hot-spot is a region of the powder bed where local heat accumulation occurs, due to an excessive energy input and a diminished heat flux towards the surrounding material (Grasso *et al.*, 2017; Colosimo and Grasso, 2018). The quick detection and localization of hot-spots is a key issue in the reduction of scrap fractions in LPBF, as hot-spots may lead to local geometrical distortions and micro-structural inhomogeneity in the manufactured part.

Figure 1 shows an example of a video-frame acquired during the LPBF of a metal part. The dark area corresponds to the background, where no action occurs. The foreground region includes:

- 1. The natural process including the Laser-Heated Zone (LHZ), i.e., the high-intensity region that includes and surrounds the zone where powder melting occurs, and the spatters generated by the laser-material interaction.
- 2. A hot-spot, i.e., the anomaly to be detected.

The LHZ displaces along the pre-defined scanning path of the laser, and its size mainly depends on the energy input. Spatters consist of either hot particles of the powder bed blown away by the metallic vapor or molten material ejected by the melt pool (Liu *et al.*, 2015; Khairallah *et al.*, 2016). Therefore, we can claim that hot-spots are sparse and clustered in the spatial domain, since when a hot-spot occurs, it stays at the same location until the affected region cools down.

Figure 1 shows that the separation of the entire image into the natural process phenomena including the LHZ, the sparse foreground events (i.e., spatters) and an out-of-control anomaly event (i.e., the hot-spot). From Figure 1 (left panel), we can conclude that using one single image to separate these events is difficult or even impossible. Therefore, the information enclosed by the temporal structure of the video-imaging data should be considered as well. Figure 1

(middle and right panels) illustrates the temporal behavior of two pixels, i.e., the time-series of their intensity within the recorded video. One pixel was located where the natural process took place, and one in a region affected by a hotspot. Figure 1 (middle panel) shows that the natural spatter and LHZ dynamics yield sudden intensity peaks in the temporal domain, which is representative of the natural temporal pattern of pixel intensities. In the presence of a hotspot, as shown in Figure 1 (right panel), however, the local heat accumulation causes the saturation of the pixel intensity and a slower cooling transitory to the background level. This is representative of the over-heating phenomena that may finally lead to a defective part. The hot-spot event can be characterized by its pixel intensity pattern in the time domain. However, this pattern can be partially "masked" by the natural patterns related to the underlying process dynamics, which makes a fast and robust detection of the hot-spot a challenging task. This motivates the use of a spatio-temporal approach, taking advantage of both spatial and temporal signatures of the anomaly.

The remainder of this article is organized as follows. Section 2 reviews the literature devoted to statistical process modelling and monitoring for video-image data. Section 3 presents the proposed methodology. In Section 4, a simulation study is used to evaluate the hot-spot detection performances. In Section 5, we compare our proposed method against benchmark techniques in the LPBF real case study. Section 6 concludes and presents future directions.

#### 2. Literature review

To address the challenge of detecting localized anomaly events in video-image data, three different categories of methods have been proposed in the literature: (i) Principal Component Analysis (PCA)-based approaches; (ii) kernel and basis representation methods; and (iii) scanning statistics techniques.

The first category includes various PCA and dimension reduction techniques suitable to reduce the dimensions of spatio-temporal data in the framework of statistical process monitoring. For example, Celik (2009) proposed a change detection algorithm for satellite image detection using PCA and K-means clustering. Various multi-variate functional PCA methods and subspace learning methods have been developed (Paynabar et al., 2013; Paynabar et al., 2016; Zhang et al., 2018, 2020) to monitor multi-channel signals. Yan et al. (2015) compared several famous tensor PCA methods for image-based process monitoring. The major drawback of the PCA-based approach is that although it assumes the low-rank structure of the spatio-temporal dataset, it neglects the locally correlated structure in images. To address this issue, an enhanced method based on a spatiallyweighted PCA formulation was proposed by Colosimo and Grasso (2018), which considers the locally correlated structures of the foreground events. However, this method does not fully utilize the sparsity structure of the anomalies, which may cause a detection delay.

The second category includes methods that attempt to model the spatio-temporal structure of an image stream by a set of known spatial or temporal basis, kernels and covariance structures. To model the smooth spatial or temporal structure of the foreground high-dimensional data for change point detection, non-parametric techniques such as local kernel regression (Zou et al., 2008; Zou et al., 2009; Qiu et al., 2010) were developed. Gaussian process regression was also proposed for video anomaly detection and representation (Cheng et al., 2015). Spatio-Temporal Smooth-Sparse Decomposition (ST-SSD) focuses on detecting sparse anomalies from the smooth spatial and temporal foreground (Yan et al., 2017, 2018). One major disadvantage of ST-SSD is that it assumes that the anomaly at each point in time is independent. However, in many applications, the anomaly event should be temporally coherent. The temporally coherent and spatially clustered structure of the anomaly is not fully considered in the aforementioned methods.

The third category includes window-based scanning methods developed to deal with anomaly detection in spatial and temporal data (Glaz et al., 2001; Neil et al., 2013). For example, scan statistics use a window-based approach to search the cluster of points in the spatial domain. However, although they are widely used for anomaly detection in scattered point patterns in 3D data, they are not necessarily suitable for spatio-temporal image streams. Other windowbased approaches for anomaly detection are developed based on low-dimensional features, such as the spatio-temporal gradient and texture information (Li et al., 2014). However, window-based approaches usually require the maximum size of the anomaly to be known in advance, which is not feasible in most applications.

The fourth group of papers in the literature is focused on using the deep learning methodology for pattern recognition in spatio-temporal data streams (Gobert et al., 2018; Scime and Beuth, 2018; Okaro et al., 2019; Sergin and Yan, 2019; Kwon et al., 2020). Techniques such as convolutional neural networks and recurrent neural networks are commonly used to model complex spatial and temporal structures in image data. However, they typically envisage a supervised learning paradigm and require a large and representative training dataset. In the present application, the geometry of the printed slice, together with the underlying dynamics of the melting process, may vary from one layer to another and from one part to another, which could make difficult to collect a labelled dataset that is sufficiently large to implement these methods.

#### 3. Proposed methodology

We first introduce the spatio-temporal decomposition and regression model in Section 3.1. In Section 3.2, we discuss how to design process monitoring statistics for monitoring and localization of the hot-spot event. For notation consistency, we use a for a scalar, a for a vector, and A for a matrix.

# 3.1. A spatio-temporal decomposition model

#### 3.1.1. Formulation

To capture the spatio-temporal structure of video-imaging data and detect anomaly events, we present the penalized non-parametric regression model and recursive estimation algorithm. We denote  $x_{s,t}$  as the intensity value of certain spatio-temporal data (e.g., signal/functional curve or videos) at location s and time t. Here, the spatial index s can be either 1D (e.g., signals or functional curves) or 2D (e.g., images). Our proposed model aims to decompose the original image/signal  $x_{s,t}$  into the background  $\mu_{s,t}$ , a natural foreground event  $u_{s,t}$ , an anomaly foreground event  $a_{s,t}$ , and noise  $e_{s,t}$  as in Equation (1):

$$x_{s,t} = \mu_{s,t} + u_{s,t} + a_{s,t} + e_{s,t}, \ s = 1,...,S, \ t = 1,...,T,$$
 (1)

where we assume that the background  $\mu_{s,t}$  is known and  $e_{s,t}$  follows an *i.i.d* normal distribution. However,  $u_{s,t}$  and  $a_{s,t}$  are unknown and should be estimated. We assume that the natural foreground event,  $u_{s,t}$ , and the anomaly event,  $a_{s,t}$ , are both sparse in the spatial domain. In addition, the anomaly event is clustered, but natural events can be either clustered or scattered.

To model the smooth temporal structure of the anomaly, e.g., a pattern like the one in Figure 1 (right panel), we propose to apply a first-order model with parameter  $\theta_s$  to model the temporal behaviour of the anomaly as  $a_{s,t} = \theta_s x_{s,t-1}$ . Therefore, combining with Equation (1), we have:

$$x_{s,t} = \theta_s x_{s,t-1} + \mu_{s,t} + u_{s,t} + e_{s,t}, \tag{2}$$

where  $u_{s,t}$  and  $\theta_s$  are the parameters to be estimated. Furthermore, the physical rationale behind the model structure is given in Online Supplemental Material Section A.

The goal is to estimate the foreground event,  $u_{s,t}$ , and the anomaly event,  $\theta_s$ , automatically from the data. We are especially interested in the anomaly event detection, i.e., when and where  $\theta_s \neq 0$ . Recall that both  $u_{s,t}$  and  $\theta_s$  should be sparse. Therefore, at each time t, we propose the penalized likelihood  $l_t(\theta, \{u_{s,t}\}_{s=1,\dots,S})$  as loss function in Equation (3). Here, we denote  $\theta$  as the vector that contains all  $\theta_s$ , defined as  $\theta = [\theta_1, \dots, \theta_S]^T$ :

$$l_{t}\left(\boldsymbol{\theta}, \{u_{s,t}\}_{s=1,\dots,S}\right)$$

$$= \left(\sum_{s,t} \|x_{s,t} - \mu_{s,t} - u_{s,t} - \theta_{s}x_{s,t-1}\|^{2} + \gamma_{1} \|u_{s,t}\|_{1}\right) +$$

$$+\gamma_{2} \|\boldsymbol{\theta}\|_{1} + \gamma_{3} \|\boldsymbol{\theta}\|_{TV} + \lambda_{0} \|\boldsymbol{\theta}\|^{2}$$
(3

where  $\sum_{s,t} \| x_{s,t} - \mu_{s,t} - u_{s,t} - \theta_s x_{s,t-1} \|^2$  is the sum of squared errors. The penalties  $\| u_{s,t} \|_1$  and  $\| \boldsymbol{\theta} \|_1$  lead to the sparse estimation of natural and anomaly events, respectively. To take the clustered structure of the anomaly into account, a further penalty term,  $\| \boldsymbol{\theta} \|_{TV}$ , defined as  $\| \boldsymbol{\theta} \|_{TV} = \| \boldsymbol{D} \boldsymbol{\theta} \|_1$  is included in the model. This penalty weights the estimated anomaly according to its spatial connectivity in the video-image domain.  $\boldsymbol{D}$  is the first-order difference matrix defined as

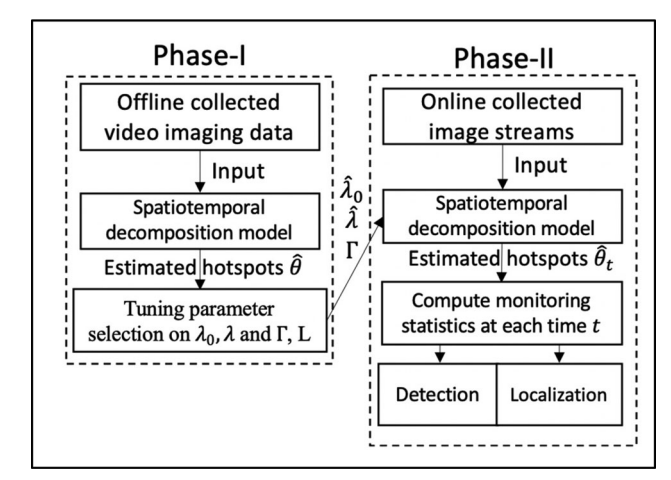


Figure 2. Flow chart of the proposed model.

$$\mathbf{D} = \begin{bmatrix} 1 & -1 & & \\ & \ddots & \ddots & \\ & & 1 & -1 \end{bmatrix}.$$

Finally, the  $\lambda_0 \parallel \boldsymbol{\theta} \parallel^2$  term is added to make the estimation robust and to solve the colinearity problem caused by the fact that large areas of each video frame, i.e., background areas, are dark with equal or very similar pixel intensities (in the case where the collinearity problem can be neglected, it is possible to get rid of this term). To aggregate the loss function  $l_t\left(\boldsymbol{\theta}, \{u_{s,t}\}_{s=1,\dots,S}\right)$  over time, a higher weight can be put on more recent data with the weight decay  $\lambda \in (0,1)$  to enable the most up-to-date estimation of the anomalies  $\boldsymbol{\theta}$ . Here,  $l_t$  only depends on  $\{u_{s,t}\}$  at time t

$$\min_{\{u_{s,t}\},\theta} L(\theta, \{u_{s,t}\}_{s=1,...,S,t=1,...,T})$$

$$= \sum_{t=1}^{T} \lambda^{T-t} l_t(\theta, \{u_{s,t}\}_{s=1,...,S})$$
(4)

# 3.1.2 Recursive estimation of the spatio-temporal process

The proposed penalized spatio-temporal regression can effectively model both the temporal and spatial structure of video-imaging data streams. However, since it is required to solve Equation (4) at each time t, an efficient optimization algorithm is needed. In this section, we propose a recursive estimation procedure to update  $\theta_s$  and  $u_{s,t}$  in a block coordinate manner.

Proposition 1 is proposed to optimize the estimation of the natural event  $u_{s,t}$  at time t in Equation (4):

**Proposition 1.** Given  $\theta_s$  in Equation (4),  $u_{s,t}$  in each time t and each point s can be solved by:

$$u_{s,t} = S\left(x_{s,t} - \mu_{s,t} - \theta_s x_{s,t-1}, \frac{\gamma_1}{2}\right),$$
 (5)



where  $S(\cdot,\cdot)$  is the soft thresholding operator defined by  $S(x, \gamma) = \operatorname{sgn}(x) \max(x - |\gamma|, 0)$ sgn(x)the sign function.

The proof is given in Online Supplemental Material Section B.

To optimize the estimation of the anomaly  $\theta$  in real-time, we ground on the following proposition:

**Proposition 2.** Given each  $u_{s,t}$  in Equation (4),  $\theta$  can be optimized by:

$$\operatorname{argmin}_{\boldsymbol{\theta}} (\| \tilde{\mathbf{\Phi}}_{T} \boldsymbol{\theta} - \tilde{\boldsymbol{\theta}}_{T} \|^{2} + \gamma_{2} \| \boldsymbol{\theta} \|_{1} + \gamma_{3} \| \boldsymbol{D} \boldsymbol{\theta} \|_{1}) , \qquad (6)$$

where

$$\tilde{\boldsymbol{\theta}}_T = \begin{bmatrix} \tilde{\boldsymbol{\theta}}_{1,T}, & \cdots, \tilde{\boldsymbol{\theta}}_{S,T} \end{bmatrix}^T, \tilde{\boldsymbol{\theta}}_{s,T} = \frac{\Psi_{s,T}}{\tilde{\boldsymbol{\Phi}}_{s,T}},$$

$$\tilde{\mathbf{\Phi}}_T = \operatorname{diag}(\tilde{\Phi}_{1,T},...,\tilde{\Phi}_{S,T}), \tilde{\Phi}_{s,T} = \sqrt{\frac{1-\lambda}{1-\lambda^T}\Phi_{s,T} + \lambda_0}.\Phi_{s,t}$$

and  $\Psi_{s,t}$  can be computed recursively as

$$\Phi_{s,t} = \lambda \Phi_{s,t-1} + x_{s,t-1}^2, \quad \Psi_{s,t} 
= \lambda \Psi_{s,t-1} + x_{s,t-1} (x_{s,t} - \mu_{s,t} - u_{s,t}), \quad (7)$$

with initialization  $\Phi_{s,1} = \Psi_{s,1} = 0$ .

The proof is given in Online Supplemental Material Section C.

It is worth noting that all coefficients including  $\Phi_{s,t}$ ,  $\Psi_{s,t}$ can be computed recursively in Equation (7), which leads to a constant updating time. To solve Equation (6), we follow the Alternating Direction Method of Multipliers (ADMM) algorithm by transforming Equation (6) to the equivalent problem:

$$\operatorname{argmin}_{\boldsymbol{\theta}} (\| \tilde{\boldsymbol{\Phi}}_{T} \boldsymbol{\theta} - \tilde{\boldsymbol{\theta}}_{T} \|^{2} + \gamma_{2} \| \boldsymbol{p} \|_{1} + \gamma_{3} \| \boldsymbol{q} \|_{1})$$
s.t.  $\boldsymbol{p} = \boldsymbol{D}\boldsymbol{\theta}, \ \boldsymbol{q} = \boldsymbol{\theta}$  (8)

The augmented Lagrangian for Equation (8) can be derived in Equation (9):

$$L(\boldsymbol{\theta}, \boldsymbol{p}, \boldsymbol{q}, \boldsymbol{y}, \boldsymbol{z}) = \|\tilde{\boldsymbol{\Phi}}_{T}\boldsymbol{\theta} - \tilde{\boldsymbol{\theta}}_{T}\|^{2} + \gamma_{2} \|\boldsymbol{q}\|_{1} + \|\boldsymbol{p}\|_{1}$$
$$-\boldsymbol{y}^{T}(\boldsymbol{p} - \boldsymbol{D}\boldsymbol{\theta}) - \boldsymbol{z}^{T}(\boldsymbol{q} - \boldsymbol{\theta}) + \frac{\rho_{p}}{2} \|\boldsymbol{p} - \boldsymbol{D}\boldsymbol{\theta}\|^{2} + \frac{\rho_{r}}{2} \|\boldsymbol{q} - \boldsymbol{\theta}\|^{2}.$$
(9)

**Proposition 3.** The ADMM algorithm derived by optimizing  $L(\theta, p, q, y, z)$  in the (k + 1)st iteration can be achieved by

$$\mathbf{y}^{(k+1)} = \mathbf{y}^{(k)} - \rho_p \left( \mathbf{p}^{(k)} - \mathbf{D}\boldsymbol{\theta}^{(k)} \right)$$
 (10)

$$z^{(k+1)} = z^{(k)} - \rho_a(q^{(k)} - \theta^{(k)})$$
 (11)

 $\boldsymbol{\theta}^{(k+1)}$  can be updated via:

$$\boldsymbol{\theta}^{(k+1)} = \left(2\tilde{\boldsymbol{\Phi}}_T^2 + \rho_q \boldsymbol{I} + \rho_p \boldsymbol{D}^T \boldsymbol{D}\right)^{-1}$$

$$\left(2\tilde{\boldsymbol{\Phi}}_T \tilde{\boldsymbol{\theta}}_T + \rho_p \boldsymbol{D}^T \boldsymbol{p}^{(k)} + \rho_a \boldsymbol{q}^{(k)} - \boldsymbol{D} \boldsymbol{y}^{(k)} - \boldsymbol{z}^{(k)}\right)$$
(12)

$$\boldsymbol{p}^{(k+1)} = S\left(\boldsymbol{D}\boldsymbol{\theta}^{(k)} + \frac{1}{\rho_p} \ \boldsymbol{y}^{(k)}, \frac{\gamma_3}{\rho_p}\right)$$
(13)

$$\boldsymbol{q}^{(k+1)} = S\left(\boldsymbol{\theta}^{(k)} + \frac{1}{\rho_q} \ \boldsymbol{z}^{(k)}, \frac{\gamma_2}{\rho_q}\right)$$
(14)

More details about the ADMM algorithm are given in Online Supplemental Material Section D.

Algorithm 1: Recursive algorithm for penalzied spatio-temporal regression

```
initialize
        u_{s,t}^{(0)} = 0
            Estimate \Phi_{s,t} = \lambda \Phi_{s,t-1} + x_{s,t-1}^2, \Psi_{s,t}^{(0)} = \lambda \Psi_{s,t-1}^{(0)} + x_{s,t-1}(x_{s,t} - \mu_{s,t}), k = 0
            for |\theta^{(k)} - \theta^{(k-1)}| > \epsilon do
                        \begin{aligned} &\boldsymbol{\theta}^{(k+1)} = (2\tilde{\boldsymbol{\Phi}}_t + \rho_q \mathbf{I} + \rho_p \mathbf{D}^T \mathbf{D})^{-1} (2\tilde{\boldsymbol{\Phi}}_T \tilde{\boldsymbol{\theta}}_T + \rho_p \mathbf{D}^T \mathbf{p}^{(k)} + \rho_q \mathbf{q}^{(k)} - \mathbf{D} \mathbf{y}^{(k)} - \mathbf{z}^{(k)}) \\ &\mathbf{p}^{(k+1)} = S(\mathbf{D}\boldsymbol{\theta}^{(k)} + \frac{1}{\rho_p} \mathbf{y}^{(k)}, \frac{\gamma_3}{\rho_p}) \\ &\mathbf{q}^{(k+1)} = S(\boldsymbol{\theta}^{(k)} + \frac{1}{\rho_q} \mathbf{z}^{(k)}, \frac{\gamma_2}{\rho_q}) \end{aligned}
                        \mathbf{y}^{(k+1)} = \mathbf{y}^{(k)} - \rho_q(\mathbf{p}^{(k)} - \mathbf{D}\boldsymbol{\theta}^{(k)})\mathbf{z}^{(k+1)} = \mathbf{z}^{(k)} - \rho_q(\mathbf{q}^{(k)} - \boldsymbol{\theta}^{(k)})
            \operatorname{end}
end
```

Finally, we show that optimizing the loss function defined in Equation (4) yields a unique global optimum in Proposition 4. This implies that no matter what initial condition we set, the model parameters will always converge to the same unique solution.

Proposition 4. Maximizing the weighted likelihood

$$\min_{\{u_{s,t}\},\boldsymbol{\theta}} L\left(\boldsymbol{\theta}, \left\{u_{s,t}\right\}_{s=1,\ldots,S,t=1,\ldots,T}\right)$$

in Equation (4) will yield to a unique global optimum of  $\theta$  and  $\{u_{s,t}\}$ .

The Proof of Proposition 4 was added in Online Supplemental Material Section E.

#### 3.1.3 Efficient computation for 2D images

All operators in Algorithm 1 have a closed-form solution and thus can be computed analytically in each iteration; however, it is still possible to further speed up the computation for the real-time implementation of the proposed approach. This section presents a few approximations that can be applied to tackle this issue. One approximation to solve Equation (12) consists of approximating  $\tilde{\Phi}_T^2$  with an identity matrix  $\tilde{\Phi}_T^2 \approx \lambda_0 I$ . Here we denote the solution of  $\theta$  for given  $\gamma_2$  and  $\gamma_3$  in Equation (6) as  $\hat{\theta}_{\gamma_2,\gamma_3}$ 

Under this approximation, it is possible to prove the following proposition (Xin *et al.*, 2014). It is worth noting that in the case where this approximation is not accurate, we can still use Algorithm 1 for the estimation of  $\tilde{\Phi}_{s,T}$  without using this approximation.

**Proposition 5.** Given  $\gamma_3 = 0$  and  $\tilde{\Phi}_T^2 = \lambda_0 I$  in Equation (12),  $\theta_s$  can be solved via soft-thresholding in Equation (15):

$$\hat{\boldsymbol{\theta}}_{\gamma_2,\gamma_3} = \boldsymbol{S}(\hat{\boldsymbol{\theta}}_{0,\gamma_3}, \gamma_2), \tag{15}$$

where  $\hat{\theta}_{\gamma_2}$ ,  $\gamma_3$  is the estimated anomaly or hot-spot coefficient under the parameter  $\gamma_2$  and  $\gamma_3$ . In particular,  $\hat{\theta}_{0,0}(t)$  is the estimated  $\theta$  when  $\gamma_2 = \gamma_3 = 0$ .

The proof of Proposition 5 can be seen in Liu et al. (2010).

Based on Proposition 5, we only need to solve a special case where  $\gamma_2=0$  as  $\hat{\boldsymbol{\theta}}_{0,\gamma_3}$ . Another advantage is that Proposition 5 allows us to efficiently solve  $\hat{\boldsymbol{\theta}}_{\gamma_2,\gamma_3}$  with multiple  $\gamma_2$ , which can be used to better design the testing statistics as mentioned in Section 3.2. Finally, we further implement an efficient approximation for block-circulant matrix as shown in Online Supplemental Material Section F.

# 3.2. Proposed process monitoring based on penalized spatio-temporal regression

In the context of Statistical Process Monitoring, also referred to as Statistical Process Control (SPC), two stages are foreseen, namely Phase I and Phase II (Oakland and Oakland, 2007). The monitoring statistic that can be used for Phase I and Phase II analysis is described in Section 3.2.1. Phase I analysis is used to estimate the in-control state (by tuning

the model parameters and designing the appropriate control limit). The detailed procedure is discussed in Section 3.2.2. Finally, the localization of the hot-spots is discussed in Section 3.2.3.

#### 3.2.1. Monitoring statistics

In this section, we describe a statistical process monitoring approach for video-imaging data that combines our proposed penalized spatio-temporal regression with a sequential LRT. Furthermore, we also discuss how the proposed method can be used for locating the anomaly after a change is detected. As we previously discussed, the goal is to detect and monitor the occurrence of the clustered anomaly event present in the spatio-temporal dataset. As mentioned, if  $\theta_s = 0$ , the pixel intensity is not auto-correlated: this condition is met under natural process conditions, where sudden spikes are caused by the natural foreground events. If  $\theta_s \neq 0$ 0, the pixel intensity is auto-correlated: this happens when the pixel stays hot (high intensity) for a long time and sudden spikes are replaced by slow cooling drifts, which is representative of the phenomenon known as a hot-spot. Finally, to incorporate the information about the estimation algorithm, instead of using the alternative hypothesis  $\theta_s \neq 0$ , we propose to use our plugin estimator  $\theta = \hat{\theta}_{\gamma_2, \gamma_3}(t)$  to replace the alternative hypothesis as  $\theta_s = \hat{\theta}_{\gamma_2,\gamma_3}(t)$ . In a high-dimensional case, using the plugin estimator has been shown to have better performance if the model is able to provide an accurate estimate of the parameter (Zou and Qiu, 2009). We are interested in signaling an event occurring in the image location s where  $\theta_s \neq 0$ . Therefore, we formulate the monitoring problem as a sequential hypothesis testing problem with the null hypothesis that no anomaly event is happening.

The rate of each point can be estimated individually as  $\hat{\theta}_{0,0}(t)$  with  $\gamma_2 = \gamma_3 = 0$ . Since we assume that an anomaly event covers just a small portion of the entire image, our proposed estimator with  $L_1$  and total variance penalty is used to accurately represent the sparse clustered structure of the anomaly. This provides an accurate estimation of the anomalous event by  $\hat{\theta}_{\gamma_2,\gamma_3}(t)$  at each time t with tuning parameters  $\gamma_2,\gamma_3$ . Therefore, at each time t, we perform the following hypothesis test:

$$H_0: \boldsymbol{\theta} = 0 \ H_1: \boldsymbol{\theta} = \delta \hat{\boldsymbol{\theta}}_{\gamma_2,\gamma_3}(t).$$

Following the procedure in Zou and Qiu (2009) and Yan et al. (2018), we can derive the testing statistic in Equation (16):

$$\tilde{T}_{\gamma_2,\gamma_3}(t) = \frac{\left(\left(\hat{\boldsymbol{\theta}}_{\gamma_2,\gamma_3}(t)\right)^{\top} \boldsymbol{\theta}_{0,0}(t)\right)^2}{\|\hat{\boldsymbol{\theta}}_{\gamma_2,\gamma_3}(t)\|^2} . \tag{16}$$

Before  $\tilde{T}_{\gamma_2,\gamma_3}$  can be used for process monitoring, the regularization  $\gamma_2,\gamma_3$  should be chosen carefully, as it plays an important role in controlling the sparsity and smoothness of  $\hat{\theta}_{\gamma_2,\gamma_3}$ . Therefore, to make the testing statistics robust to tuning parameter selection, the modified testing statistic is



defined as:

$$\tilde{T}(t) = \max_{(\gamma_1, \gamma_2, \gamma_3) \in \Gamma} \frac{\tilde{T}_{\gamma_2, \gamma_3}(t) - E(\tilde{T}_{\gamma_2, \gamma_3})}{\sqrt{Var(\tilde{T}_{\gamma_2, \gamma_3})}} . \tag{17}$$

Here, the mean and variance of the  $T_{\gamma_2,\gamma_3}$  can be estimated by the sample mean and sample variance of  $T_{\gamma_2,\gamma_3}$ from the In-Control (IC) data. Finally, we choose a control limit L > 0 for Equation (8) and if T(t) > L, the monitoring scheme would trigger an Out-Of-Control (OOC) alarm at time t. Let  $\Gamma$  be the set of parameters  $(\gamma_1, \gamma_2, \gamma_3)$ . The selection of the tuning parameter, the control limit L, and other parameters is discussed in Section 3.2.2.

#### 3.2.2. Tuning parameter selection

In this section, we discuss how to select tuning parameters  $\gamma_1, \gamma_2, \gamma_3, \lambda_0, \lambda$ , and the control limit L. First, we would like to clarify the role of each tuning parameter. As previously mentioned,  $\gamma_1$  controls the sparsity of the foreground, whereas  $\gamma_2$  and  $\gamma_3$ , respectively, control the sparsity and the smoothness of the hot-spots. The challenge in selecting the parameters  $\gamma_2$ ,  $\gamma_3$  is that it is often hard to predict the magnitude of the hot-spot. Also, it is not easy to predict the level of sparsity in the foreground. Therefore, we propose a technique to combine multiple tuning parameters  $(\gamma_1, \gamma_2, \gamma_3)$ in a way to reduce the sensitivity of the method to their values and to enhance the overall performances. This technique has been used in some previous work including Zou and Qiu (2009) and Yan et al., (2018).

In this study, we denote the set of parameters  $(\gamma_1, \gamma_2, \gamma_3)$ 

$$\begin{split} \Gamma = \left\{ \left( \frac{\gamma_{1max}}{n_{\gamma_1}} j_1, \frac{\gamma_{2max}}{n_{\gamma_2}} j_2, \frac{\gamma_{3max}}{n_{\gamma_3}} j_3 \right), j_1 = 0, ..., n_{\gamma_1}, \\ j_2 = 0, ..., n_{\gamma_2}, \ j_3 = 0, ..., n_{\gamma_3} \right\}, \end{split}$$

where  $\gamma_{1max}$  can be selected when  $\hat{u} = 0$ ,  $\gamma_{2max}$  can be selected as the  $\gamma_2$  value that results in  $\hat{\theta}_{\gamma_2,0} = 0$ , and  $\gamma_{3max}$ can be selected as the  $\gamma_3$  value resulting in  $\hat{\theta}_{0,\gamma_3}=c$ . The binary search algorithm can be used to find the values  $\gamma_{1max}, \gamma_{2max}, \gamma_{3max}$ . Furthermore, Proposition 3 can be used to efficiently compute the  $\hat{\theta}_{\gamma_2,\gamma_3}$  under different  $\gamma_2$  values without re-running the algorithm. The next problem is to select a reasonable value for  $n_{\gamma_2}$  and  $n_{\gamma_3}$ . In general, larger values of  $n_{\gamma_2}$  and  $n_{\gamma_3}$  may lead to a better detection power, but they also yield a higher computational effort. In our experiments, we selected  $n_{y_1} = n_{y_2} = 5$  and  $n_{y_3} = 2$  to balance the computational effort and detection power.

Similar to the ridge regression or elastic net, selecting a non-zero  $\lambda_0$  for the  $L_2$  penalty is especially helpful for the case of large colinearity. For example, selecting a larger  $\lambda_0$  would always result in a smaller  $\theta$ . Therefore, we propose to select  $\lambda_0$ as a tool for false positive control. We propose to select  $\lambda_0$  such that the falsely detected hot-spot events takes roughly about 5% of all the pixels when the proposed method is applied to IC data, but smaller percentages could be applied too.

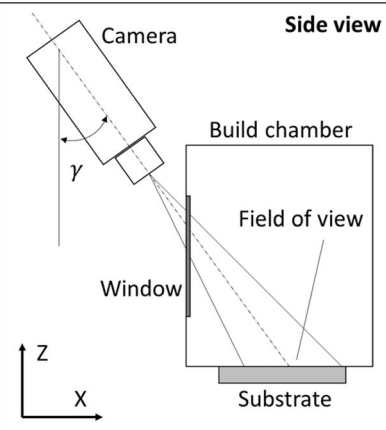
Finally,  $\lambda \leq 1$  is the weight parameter that shows the decay of the samples contribution over time. In practice, a larger  $\lambda$  will result in all the past samples to be included in the estimation with equal weights, which is useful to detect a change of small magnitude. However, if the change magnitude is larger, a larger  $\lambda$  may result in a large detection delay. The selection of  $\lambda$  follows the same philosophy of selecting the weight parameter in exponentially-weighted moving average control charts (Lu and Reynolds Jr, 1999). Additional details about how  $\lambda$  would affect the detection power are discussed in the simulation study where we propose a simulation procedure of finding the exact  $\lambda$  value. In general, if we manually add the anomaly with the estimated cooling rate, the  $\lambda$  with the shortest detection delay will be chosen. In the simulation study, we find that  $\lambda = 0.3$  is a reasonable choice.

Finally, we can choose the control limit L > 0 to achieve a given IC average run length (ARL). Some numerical search algorithms, such as bisection search, can be applied to select L (Zhang et al., 2018).

#### 3.2.3. Localization of detected changes

After the proposed control chart triggers an OOC signal, the next step consists in identifying where the anomalous event has occurred. This information can be used to identify regions of the manufactured part where a defect originated during the process and for diagnosis purposes.





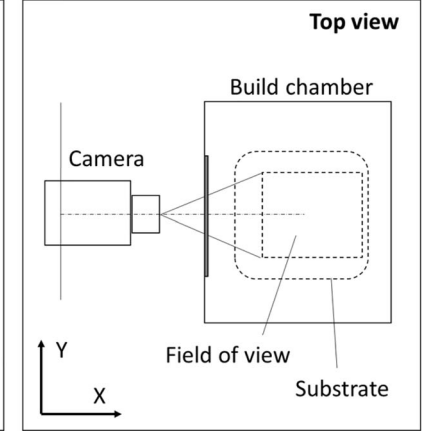


Figure 3. Experimental setup used for high-speed video imaging with OlympusTM I-speed 3 camera placed outside a commercial Renishaw® AM250 system.

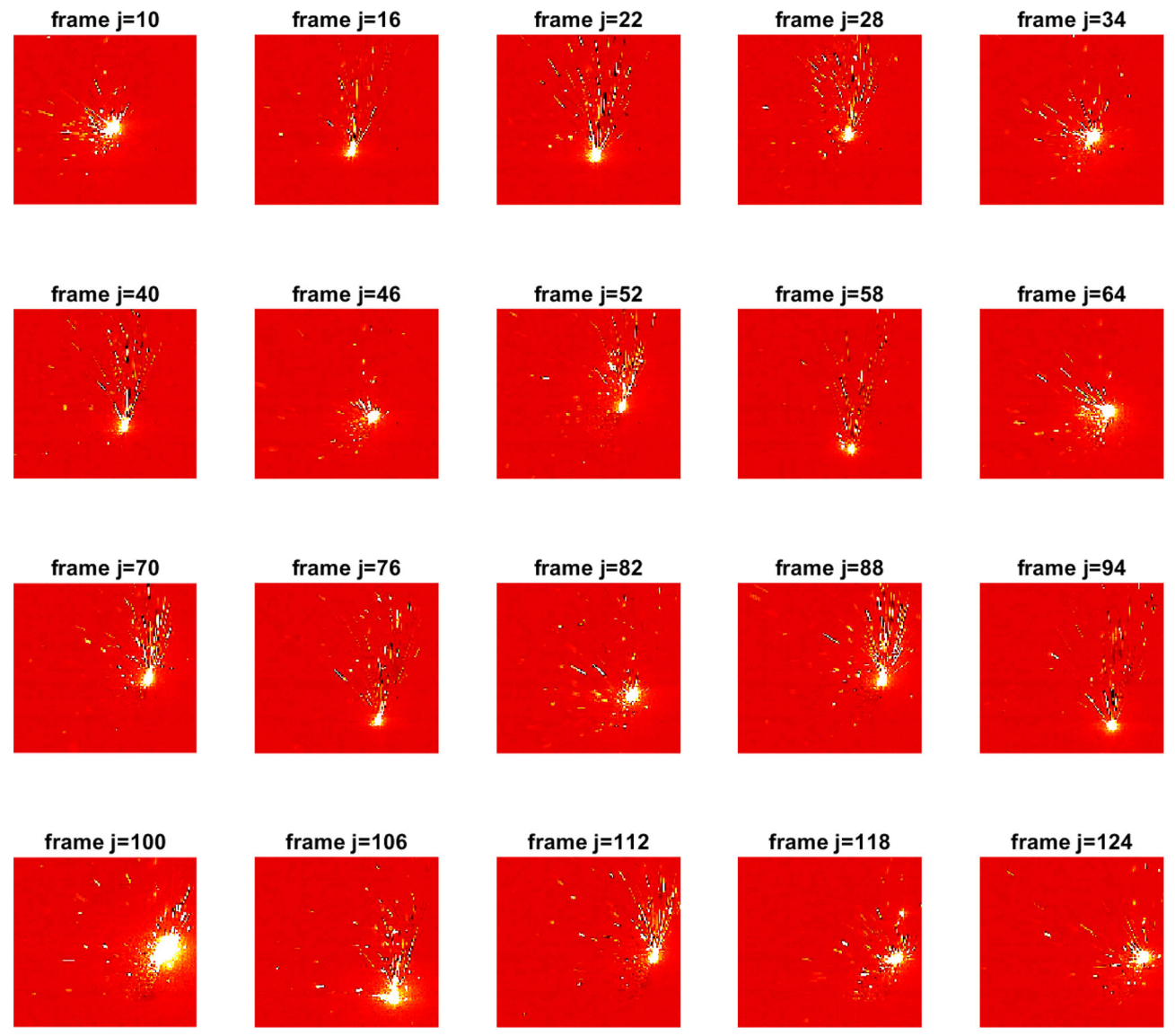


Figure 4. Examples of video frames (in false colors) acquired during the LPBF of a cylindrical part used as a reference for the generation of simulated hotspot events.

Suppose the control chart triggers a signal at time  $\tau$ . We will first find the best set of  $(\gamma_1, \gamma_2, \gamma_3)$ , which optimizes Equation. (16). Finally, the non-zero elements of the corresponding  $\hat{\boldsymbol{\theta}}_{\gamma_2, \gamma_3}$  can be used to identify the location of the anomaly event.

Finally, Figure 2 shows a flowchart to guide the practitioners in the implementation and use of the proposed algorithm. In Phase I analysis, a set of images without the anomaly can be collected. These images can also be a video stream recorded previously or an initial set of video images of the same video stream. We would like to clarify that Phase I analysis can be carried out in two different ways. It can be based on video-image data acquired during the production of a sample whose properties are representative of the shape of the part to be produced or it can be based on video-image data acquired during a few initial layers of the same part. The first approach is more convenient in the presence of a serial production of parts with equal geometry or with analogous

geometrical features. The second approach is more convenient in a one-of-a-kind application. Even if the geometry and scanning path may change from layer to layer, both natural and anomaly patterns are always characterized by similar dynamics. This allows the use of some initial layers to train the model and then the use of the same model to monitor the process in all following layers as shown in our case study.

Through this Phase I analysis, due to the natural dynamics of the process, an incorrect choice of tuning parameters may lead to excessive false alarm rates. Therefore, during Phase I, tuning parameters  $\lambda_0$ ,  $\lambda$ ,  $\Gamma$ , L are selected to achieve a false alarm rate for falsely identified hotspot  $\hat{\theta}$  corresponding to the target one. During Phase II, the current video-image stream is used as input to the spatio-temporal model to estimate the hot-spot  $\theta_t$ . The estimated hot-spot can be used to compute the monitoring statistics by combining multiple tuning parameters  $\Gamma$  for online monitoring and anomaly detection.

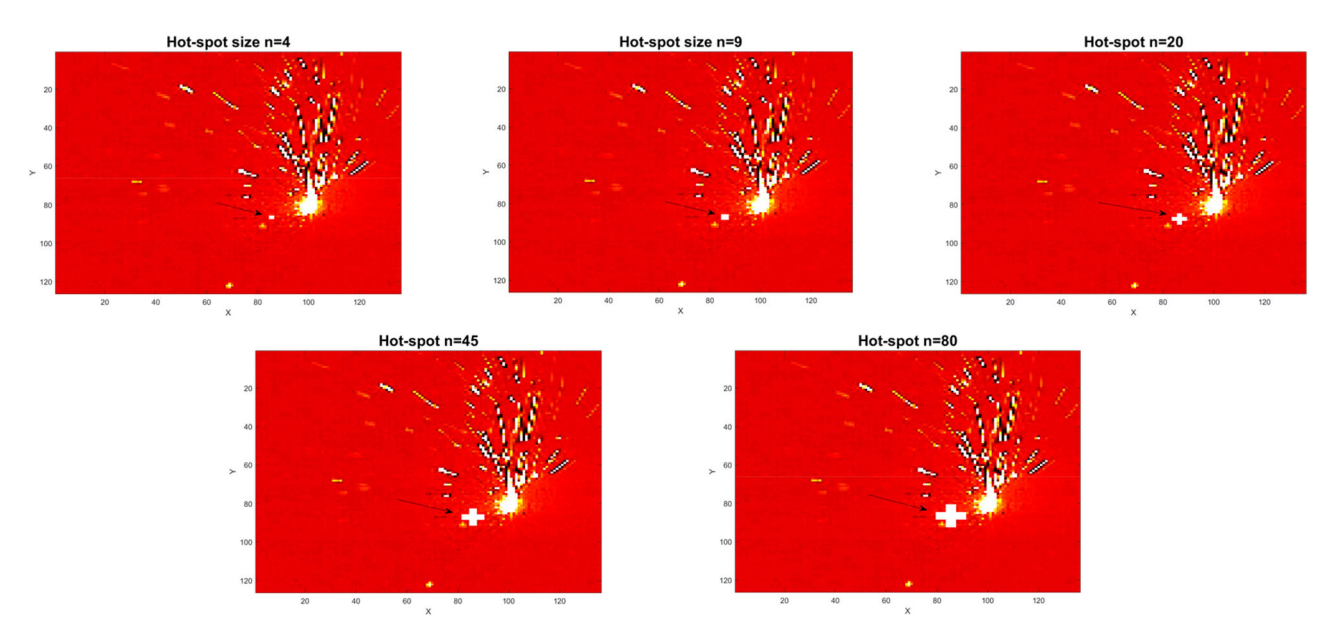


Figure 5. Examples of one original video frame (false colors) with an injection of simulated hot-spot of different sizes.

## 4. Simulation analysis

In this section, we will use a simulation analysis to evaluate the performance of the proposed algorithm. The simulation was carried out by artificially injecting hot-spot events in different locations and with different sizes into a real video-image stream acquired during an IC LPBF process. More details about the simulation setup are presented in Section 4.1. We then discuss the performance evaluation of the proposed method against benchmark methods in Section 4.2. Finally, a sensitivity analysis of how the tuning parameters would affect the methodology is presented in Section 4.3.

#### 4.1. Simulation setup

A cylindrical shape of diameter 16 mm was produced via LPBF of AISI 316L powder (average particle size of about 25-30 μm) on a Renishaw® AM250 system. The post-process inspections of the as-built part allowed judging the process as being IC and the part as defect-free. A 150 fps video-sequence was acquired during the realization of one layer of the part by using the setup shown in Figure 3, which consists of an OlympusTM I-speed 3 camera (CMOS sensor) mounting a 50 mm lens placed outside the build chamber's viewport. The camera setup used in our real case study may induce a distortion caused by the perspective angle, which was corrected by means of a perspective correction operation carried out in the calibration phase. A further nuisance effect caused by this setup is the possible presence of bright spots corresponding to reflections of the LHZ on the viewport window. The image acquisition settings were selected in order to minimize this effect. In the experiments, due to the high-speed video imaging setup, the integration time is so short that, when the laser is turned off a fully dark frame is acquired (slight pixel intensity variations are simply due to the signal noise). This means that the external lighting conditions do not affect the video

**Table 1.** Average values of performances indexes for different methods and different hot-spot sizes (the standard deviation of mean values is reported in parentheses).

purchateses <sub>j</sub> .									
Hot-spot size	Method	ARL	Precision	Recall	F-score				
Small ( <i>n</i> = 4)	Proposed T-square PCA Tucker Lasso Fused Lasso ST-SSD ST-PCA	<b>3.39 (1.57)</b> 75.31 (47.01) 87.66 (49.48) 77.21 (47.97) 90.51 (49.12) 100.07 (46.45) 77.28 (53.90) 73.19 (1.57)	0.88 (0.27) 0.01 (0.01) 0.00 (0.01) 0.01 (0.01) 0.01 (0.01) 0.00 (0.00) 0.00(0.00) 1.00 (0)	0.98 (0.14) 0.33 (0.47) 0.30 (0.43) 0.60 (0.35) 0.23 (0.42) 0.28 (0.45) 0.35 (0.47) 1.00 (0)	0.90 (0.24) 0.01 (0.02) 0.01 (0.01) 0.01 (0.01) 0.00 (0.00) 0.00 (0.00) 0.01(0.01) 1.00 (0)				
Med-small (n = 9)	Proposed	2.65 (1.14)	0.91 (0.19)	0.98 (0.14)	0.94 (0.17)				
	T-square	75.31 (47.01)	0.01 (0.02)	0.34 (0.47)	0.02 (0.03)				
	PCA	81.96 (49.16)	0.01 (0.02)	0.35 (0.45)	0.02 (0.03)				
	Tucker	75.31 (47.60)	0.01 (0.02)	0.61 (0.30)	0.02 (0.03)				
	Lasso	84.81 (49.49)	0.01 (0.02)	0.41 (0.46)	0.01 (0.00)				
	Fused Lasso	83.91 (49.07)	0.00 (0.00)	0.40 (0.49)	0.00 (0.01)				
	ST-SSD	72.74 (54.94)	0.00(0.00)	0.46 (0.50)	0.01(0.01)				
	ST-PCA	68.33 (2.10)	1.00 (0)	1.00 (0)	1.00 (0)				
Medium ( <i>n</i> = 20)	Proposed	2.29 (0.78)	0.97 (0.11)	0.99 (0.10)	0.98 (0.10)				
	T-square	81.01 (46.65)	0.02 (0.04)	0.29 (0.45)	0.04 (0.07)				
	PCA	84.81 (47.61)	0.02 (0.03)	0.31 (0.43)	0.04 (0.06)				
	Tucker	68.10 (45.90)	0.03 (0.04)	0.60 (0.26)	0.05 (0.07)				
	Lasso	85.76 (47.75)	0.02 (0.04)	0.52 (0.45)	0.04 (0.08)				
	Fused Lasso	58.25 (47.07)	0.02 (0.05)	0.63 (0.48)	0.04 (0.09)				
	ST-SSD	59.62 (57.87)	0.01(0.00)	0.60 (0.49)	0.02 (0.00)				
	ST-PCA	63.08 (2.27)	0.94 (0.01)	1.00 (0)	0.97 (0.01)				
Med-large (n = 45)	Proposed	2.01 (0.52)	0.98 (0.10)	0.99 (0.10)	0.98 (0.10)				
	T-square	80.21 (49.48)	0.05 (0.08)	0.32 (0.47)	0.09 (0.13)				
	PCA	83.00 (48.66)	0.05 (0.07)	0.32 (0.44)	0.08 (0.12)				
	Tucker	41.09 (42.54)	0.10 (0.07)	0.61 (0.22)	0.17 (0.12)				
	Lasso	54.56 (46.83)	0.14 (0.12)	0.74 (0.37)	0.22 (0.19)				
	Fused Lasso	36.33 (39.83)	0.16 (0.19)	0.75 (0.43)	0.24 (0.26)				
	ST-SSD	37.09 (47.73)	0.02(0.00)	0.81 (0.39)	0.04 (0.01)				
	ST-PCA	58.39 (2.43)	0.88 (0.01)	<b>0.99 (0.003)</b>	0.93 (0.01)				
Large (n = 80)	Proposed	1.20 (0.58)	0.87 (0.16)	0.99 (0.10)	0.92 (0.13)				
	T-square	65.03 (50.77)	0.14 (0.14)	0.50 (0.50)	0.22 (0.22)				
	PCA	74.50 (53.21)	0.12 (0.14)	0.46 (0.47)	0.19 (0.21)				
	Tucker	9.47 (12.54)	0.28 (0.09)	0.64 (0.22)	0.38 (0.11)				
	Lasso	36.73 (45.28)	0.33 (0.20)	0.75 (0.43)	0.45 (0.27)				
	Fused Lasso	27.60 (33.02)	0.25 (0.28)	0.79 (0.41)	0.32 (0.33)				
	ST-SSD	45.75 (53.82)	0.04(0.00)	0.61 (0.42)	0.07 (0.02)				
	ST-PCA	65.76 (2.07)	0.83 (0.01)	0.96 (0.01)	0.89 (0.01)				

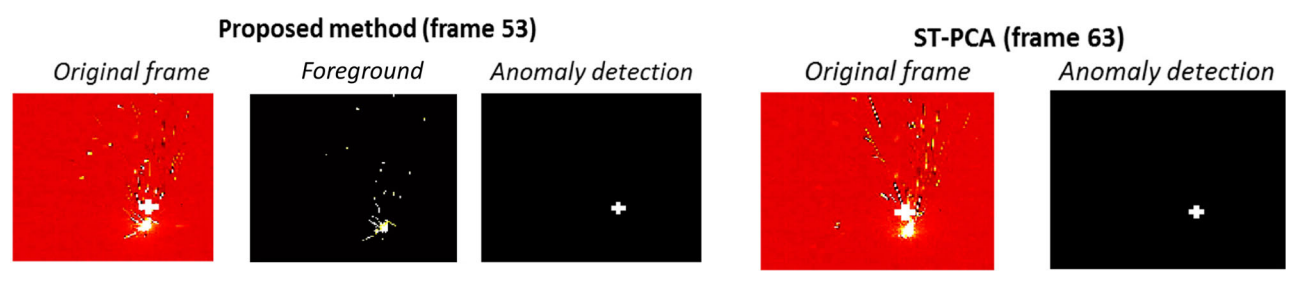


Figure 6. Example of signals from different algorithms in one simulation run; Methods not shown in the figure did not signal in the considered simulation run, and foreground not shown for ST-PCA given it is not a decomposition-based method.

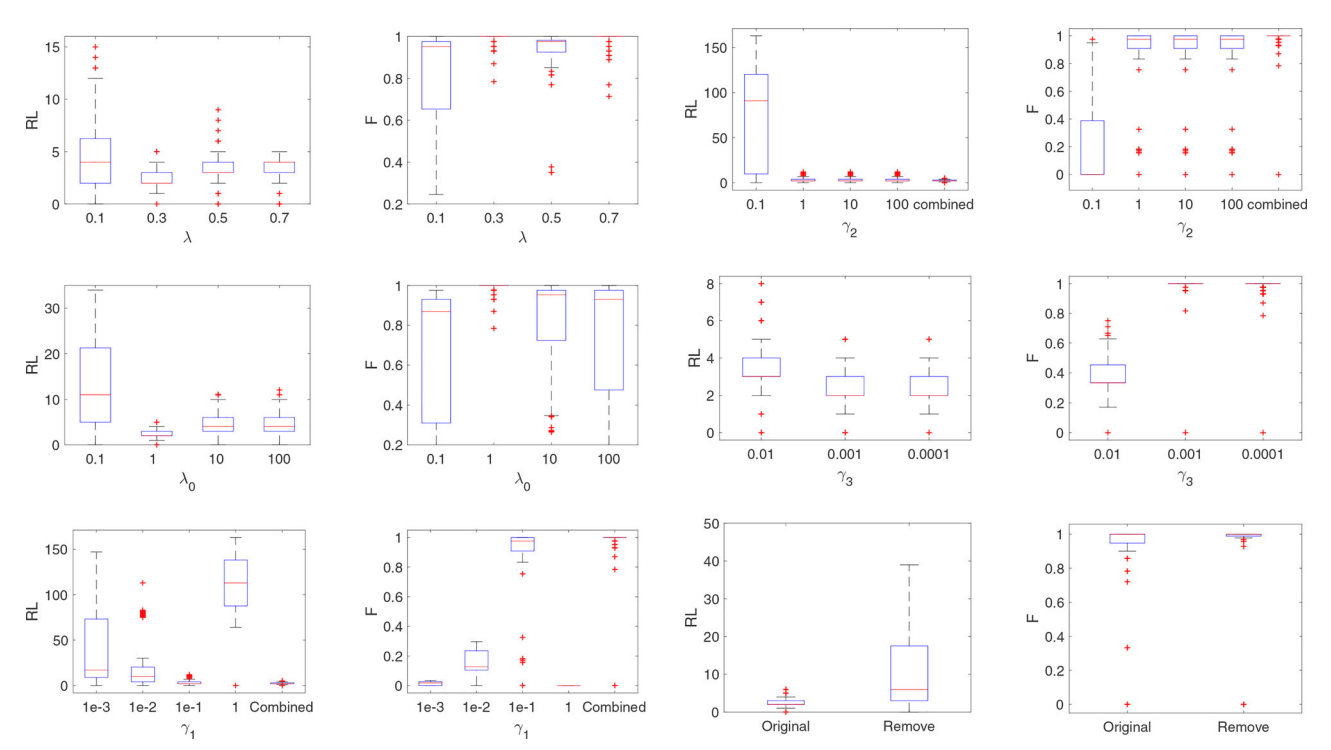


Figure 7 (Left) - Sensitivity analysis of how  $\lambda$  (1st row),  $\lambda_0$  (2nd row),  $\gamma_1$  (3rd row). (Right) Sensitivity analysis of how  $\gamma_2$  (1st row),  $\gamma_3$  (2nd row), and the LHZ removal pre-processing step (3rd row) affect the RL and the F-score.

images. Additional details about the experimental setup and the LPBF process are discussed in Colosimo and Grasso (2018).

As an example, Figure 4 shows a subset of the original video frames, where a circular slice of the vertical cylinder was produced. The frame size was 126 x 136 pixels.

Hot-spots were simulated at 100 different locations. The simulation was conceived to generate the onset in a realistic way, starting just after a laser scan in the selected location and lasting for  $\tau$  consecutive frames. For each location, the hot-spot duration  $\tau$  was varied in different simulation runs, ranging from  $\tau>1$  to  $\tau=180$  consecutive frames. We simulated only one hot-spot at a time. In principle, multiple hot-spots can be present in the same monitored area. The proposed method is not constrained to detect a single hot-spot event, but future analysis may be carried out to test its performance in the presence of multiple hot-spots. Hot-spots of different sizes were simulated, affecting a number of clustered pixel n equal to 4, 9, 20, 45 and 80.

An example of one video frame where simulated hotspots with different sizes were injected is shown in Figure 5.

In the simulations, a cross-shaped hot-spot was injected to simplify the visual identification of the anomaly in the video frames.

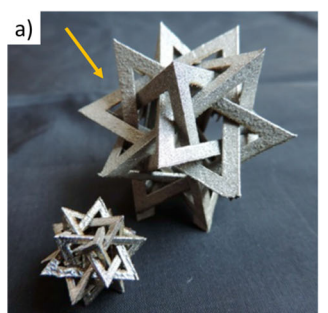
The simulated hot-spot consists of a saturated intensity  $(a_{s,t} = 255)$  for several consecutive frames followed by a slow cooling transitory (i.e., a pixel intensity decrease) to the average background intensity. A sigmoid function was used to generate this pattern, accordingly to the following expression:

$$a_{s,t} = \frac{255}{1 + \exp(0.2(t - H\tau))}, \ t = 1, ..., \tau,$$
 (18)

where H is a constant that controls the shape of the cooling profile in the hot-spot regions. Equation (18) with H=0.95 was used in this study to generate a realistic hot-spot pattern over time. We refer the reader to Colosimo and Grasso (2018) for additional details.

#### 4.2 Performance evaluation

We compared the proposed method against four benchmark methods available in the literature. The first benchmark



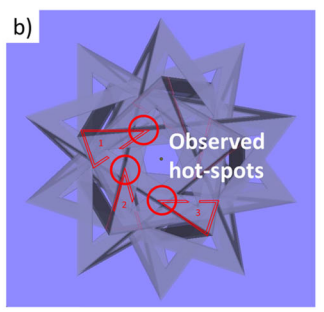




Figure 8. (a) Complex shape part used to test the proposed approach; (b) examples of triangular portions of the sliced CAD model; and (c) local defects corresponding the acute corners of those triangles.

Table 2. Main process parameters used in the experimental activity.

	Laser power (P)	Exposure time (t)	Focus position $(f_p)$	Point distance $(d_p)$	Hatch distance $(d_h)$	Layer thickness (z)
Value	200 W	80 μs	0 mm	60 μm	110 <i>μ</i> m	50 μm

approach is Hoteling's T<sup>2</sup> control chart (Hotelling, 1992) (denoted as "T2"), applied to the vectorized frames of the video, where each pixel is treated as a variable and each frame as a new observation. This is representative of a basic control charting scheme that can be applied to video-images by practitioners. The second benchmark method is a PCAbased control chart applied to vectorized images (Nomikos and MacGregor, 1995). This is representative of the S-mode PCA-based approach mentioned in Colosimo and Grasso (2018) and it is representative of the basic way to apply the PCA to video-imaging data (denoted as "PCA"). The third benchmark method is the Tucker decomposition, which is the tensor-version of the PCA methods (denoted as "Tucker"), which is detailed in Yan et al. (2015). The fourth benchmark method consists of a Lasso-based control chart (denoted as "Lasso"). In this case, we implemented the procedure proposed by Zou and Qiu (2009), in which Lasso (Tibshirani, 1996) is used to first identify the sparse change direction and the LRT is applied for change detection and anomaly identification. The fifth benchmark method is the Fused-Lasso-based control chart, which considers the spatial continuity of the proposed method (Liu et al., 2010) (denoted as "Fused Lasso"). The sixth benchmark method is based on the ST-SSD to separate the anomaly event from the background events (Yan et al., 2018). The last benchmark method is the spatially weighted T-mode PCA (denoted as "ST-PCA"), proposed by Colosimo and Grasso (2018). This is representative of the current state-of-the-art methodology for hot-spot detection in LBPF via in-situ video-imaging. In the T-mode PCA formulation (Jolliffe, 2002; Tsutsumida et al., 2017), the video frames are treated as variables and image pixels as observations. This allows one to capture the temporal auto-correlation of pixel intensities over consecutive frames. The underlying idea of the spatially weighted T-mode PCA consists of incorporating the pixel spatial correlation into the projection operation entailed by the T-mode PCA. The resulting ST-PCA was combined with a recursive updating scheme to iteratively include new video frames for in-line hot-spot detection. A k-means clustering-based alarm rule was eventually

proposed to signal an alarm in the presence of a region of the image where the hot-spot event occurred. For T2, PCA and Lasso, since the algorithms cannot handle the temporaldependent dynamics of the LHZ, they rely on a pre-processing step that consists of removing the largest connected component corresponding to the LHZ from each frame. For all the methods, we selected the control limit based on the IC samples with the false positive rate of 0.01.

The performances of compared methods were estimated by means of different metrics. The ARL was used to quantify how fast each method can detect the hotspot. Precision and recall scores were used to quantify the localization accuracy when the defect is detected (Powers, 2020). The precision score can be defined as the ratio between the pixels belonging to the hot-spot region that were correctly detected by the monitoring method and the overall number of detected pixels. A precision score that is equal to one means that the monitoring method detected only hot-spot pixels, and hence, no false alarm outside the hot-spot region is produced. The recall score can be defined as the ratio between the pixels belonging to the hot-spot region that were correctly detected by the monitoring method and the overall number of pixels belonging to the hot-spot. A recall score equal to one1 means that the monitoring method can detect the entire hot-spot region, and hence, no false negative is present. One additional metric was considered: it is the F-score, which is the harmonic mean of the precision and recall score (Rijsbergen, 1979). Table 1 summarizes the comparison between the proposed approach and all other competing methods in the presence of simulated hot-spots of different sizes.

The data in Table 1 highlights that the proposed method is much faster than all the other methods in detecting the hot-spot. In terms of ARL, the proposed method can detect the hot-spot in less than three or four frames from the hotspot event injection for all simulated sizes. The reason for this delay is that the onset of real hot-spots occurs in locations where the laser beam has just scanned and melted the area. During the time that the LHZ overlaps the hot-spot location, no detection is possible. However, when the LHZ

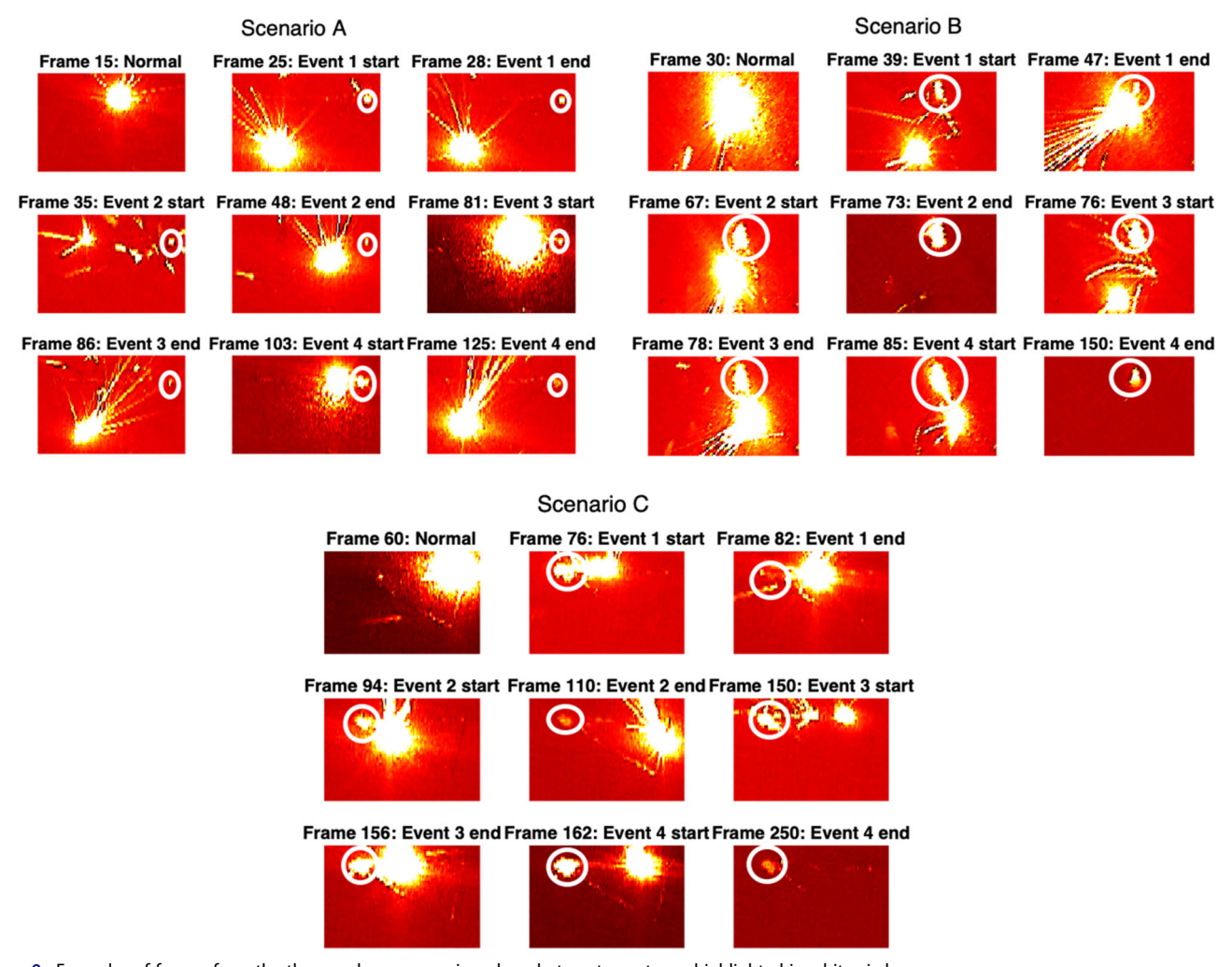


Figure 9. Examples of frames from the three real-case scenarios where hot-spot events are highlighted in white circles.

moves away following the predefined laser path, detection becomes possible. It is also clear that a larger hot-spot will result in a shorter detection delay. On the contrary, no other method was able to signal the hot-spot in less than between 50 and 60 frames since its onset. Indeed, competitor methods require a sufficient number of frames before the observed patterns in the temporal and/or spatial domain can be signalled as anomalous with respect to the natural process dynamics. The proposed approach, instead, entails a model of both the natural and OOC patterns that may arise in the video-imaging data. Therefore, the hot-spot event can be detected since its onset stage, as its occurrence yields a sudden shift of the corresponding parameter in the spatio-temporal model.

In terms of hot-spot localization accuracy, the Hotelling's  $T^2$  control chart, the basic PCA-based approach, the Lasso-based control chart, and ST-SSD are not only slower than the proposed approach in detecting the hot-spot, but also they are also less accurate. The precision score of these three competitors is always very low, which means that they signal as being OOC a large portion of the video frame. This makes these methods ineffective in the present application. The  $T^2$  control chart, the PCA-based control chart, and tensor-PCA-based control chart fail because they focus on

detecting a global variation of video-imaging data patterns, whereas the hot-spot event is local in nature, with a reduced effect on both the average pixel intensity and the global variability. On the other hand, the Lasso-based and Fused-Lasso-based control charts allow dealing with the spatial structure of video frames, and hence, they are potentially able to detect local events. However, as discussed in Section 1, the spatial information alone may not be sufficient to distinguish the hot-spot event from other natural foreground events, i.e., the LHZ and the spatters generated by the laser-material interaction. Indeed, the Lasso-based control chart and fused-Lasso-based control chart fail because they do not consider any temporal structure of the video-imaging data. The performance of ST-SSD is quite poor. ST-SSD assumes that the background is smooth and the anomaly is an abrupt change, which violates our assumption that the background is random, but the anomaly is spatially clustered and temporally consistent. The ST-PCA methodology yields comparable and accurate results in localizing the hot-spot, but it requires a sufficient number of video frames to properly identify an anomalous auto-correlation pattern in the pixel intensities within the hot-spot region. Moreover, in the presence of the largest simulated hot-spot event, the performances of the ST-PCA based methodology were slightly

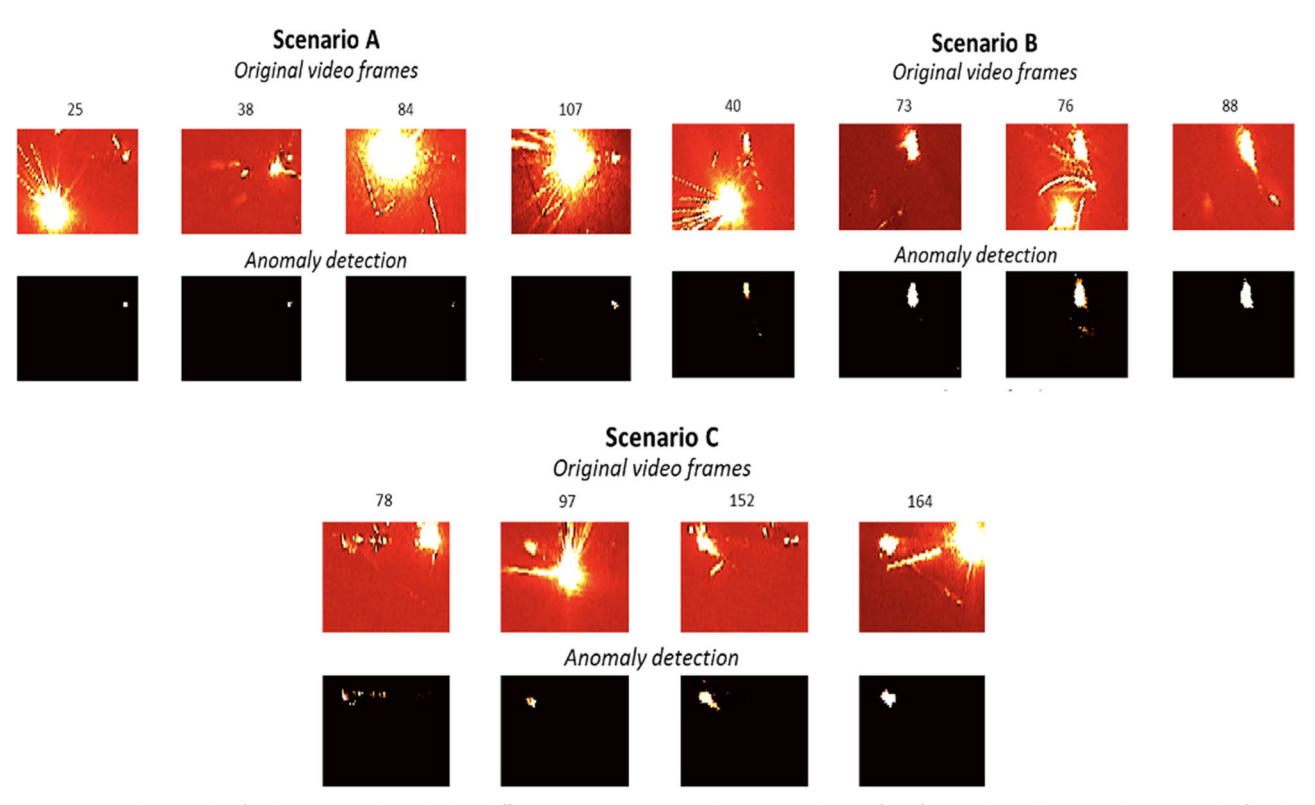


Figure 10. Detected anomalies for the proposed method in different scenarios; For each scenario, the top four figures show the original images. The four bottom figures show the detected anomalies, where the anomaly location is shown in white.

worse than those for smaller hot-spots. Indeed, when the hot-spot becomes larger, the overlap between the hot-spot itself and the LHZ increases, reducing the capability to distinguish the two regions into two separate clusters. This issue does not affect the proposed method, whose performance improves as the hot-spot size increases.

Figure 6 shows the detected anomalies for different methods in one simulation run. In that run, only the proposed method, the ST-PCA, and Fused Lasso signaled an alarm. For the proposed method (top row), Figure 6 (left panels) shows original images corresponding to the video frames where an alarm was signaled. Figure 6 (middle panels) shows the foreground separated by the proposed method. Figure 6 (right panels) shows the regions of the frames (white) signaled as a detected anomaly. In Figure 6, both the proposed method and ST-PCA detect the location of anomalies accurately, the proposed method, however, was faster in detecting the hot-spot event (frame 53, whereas the ST-PCA method signaled at frame 63). The proposed method is the only one that is able to estimate the foreground event, due to the decomposition framework proposed. Finally, we also perform another analysis on how many consecutive anomalous samples are needed to detect the anomaly and the results are presented in Online Supplemental Material Section G.

# 4.3. Sensitivity analysis

To understand how the tuning parameter selection  $\lambda$ ,  $\lambda_0$  and pre-processing procedure affects the result, Figure 7 shows how they affect the run length and the F-score for the

Table 3. Performances indexes for different methods in different real case study scenarios.

			Time of first signal (frame index)				
Scenario			Event 1	Event 2	Event 3	Event 4	
A	Actual onset of hot-spot event		25	35	81	103	
	Competing methods	Proposed	25	38	84	107	
		T-square	_	40	84	_	
		PCA	_	_	-	_	
		Tucker	_	_	85	167	
		Lasso	_	_	-	165	
		Fused Lasso	_	45	85	167	
		ST-SSD	-	_	_	167	
		ST-PCA	-	40	81	103	
В	Actual onset of hot-sp	pot event	39	67	<i>75</i>	85	
	Competing methods	Proposed	40	72	76	88	
		T-square	_	_	77	_	
		PCA	-	_	77	_	
		Tucker	-	-	77	-	
		Lasso	-	_	77	_	
		Fused Lasso	-	_	77	_	
		ST-SSD	_	_	-	-	
		ST-PCA	-	_	-	94	
C	Actual onset of hot-sp	pot event	77	94	150	162	
	Competing methods	Proposed	78	97	152	164	
		T-square	_	_	152	_	
		PCA	-	_	_	168	
		Tucker	80	_	150	168	
		Lasso	_	_	153	_	
		Fused Lasso	78	_	152	168	
		ST-SSD	_	_	-	168	
		ST-PCA	_	_	-	164	

medium size hot-spot (n = 20) in our simulation. We can clearly see that different choices of  $\lambda$  does have an impact on the Run Length (RL) and localization accuracy (F-score). Too small values of  $\lambda$  (e.g.,  $\lambda = 0.1$ ) lead to worse localization accuracy (F-score much smaller than one) since too

Table 4. The computation time of all methods.

	Proposed	T-square	PCA	Tucker	Lasso	Fused Lasso	ST-SSD	ST-PCA
Time (s)	0.01	0.0002	0.004	0.002	0.001	0.03	0.006	0.28
Standard deviation (s)	0.0033	0.0004	0.001	0.001	0.0004	0.01	0.003	0.045

large a weight is given to the most recent sample. However, too large values of  $\lambda$  (e.g.,  $\lambda = 0.7$ ) lead to a good localization accuracy, but also increase the detection delay, since a lower weight is given to the most recent samples. Similarly, too small values of  $\lambda_0$  (e.g.,  $\lambda_0 = 0.1$ ) lead to a much larger variance of the algorithm, due to the potential overfitting. Too large values of  $\lambda_0$  (e.g.,  $\lambda_0 = 10,100$ ) cause a strong under-estimation of the anomaly, due to the shrinkage effect. In the present application, we advocate the implementation of the proposed approach to the original images with  $\lambda = 0.3$  and  $\lambda_0 = 1$ .

Furthermore, we also study how the regularization parameters  $\gamma_1, \gamma_2, \gamma_3$  would affect the results. Figure 7 shows that too small values of  $\gamma_1$  (e.g.,  $\gamma_1 < 1e - 2$ ) could give too much flexibility in the foreground event estimation, and some anomalies and noise could be misclassified as the foreground event. However, too large values of  $\gamma_1$  (e.g.,  $\gamma_1 > 1$ ) could also cause an under-estimation of the foreground event, and these random foreground events could then lead to a worse estimation of the anomaly too. For  $\gamma_2$ , as long as it is set larger than one, the detection delay and accuracy are not greatly influenced. Finally, the combined procedure of using multiple  $\gamma_1$ ,  $\gamma_2$  is suggested since it greatly reduces the RL and increases the F-value compared with using any  $\gamma_1$  or  $\gamma_2$  values. Finally, we found the algorithm to be relatively robust to  $\gamma_3$  unless  $\gamma_3$  is too large. This is because too large values of  $\gamma_3$  (e.g.,  $\gamma_3 > 0.01$ ) may put too large a smoothness penalty on the anomaly, which leads to the under-estimation of small anomalies.

Finally, we also investigated whether the LHZ removal pre-processing step can affect the performance of the proposed algorithm. Figure 7 (right panels) show that, when such a pre-processing step is applied, the proposed algorithm typically yields a larger RL. The reason is that the implemented LHZ removal operation might sometimes accidentally also remove the hot-spot, which inflates the OOC detection delay. Despite this, the LHZ removal operation slightly increases the accuracy of the hot-spot localization, as a partial overlap between the LHZ and the hot-spot is avoided.

#### 5. Case study

In this section, we will evaluate the performance of the proposed algorithm using a case study that considers a real LPBF process with three different settings. The real case study was previously presented in Grasso et al. (2017) and Colosimo and Grasso (2018). It was selected to address a real production scenario, where all process parameters are kept fixed, but hot-spots are produced by critical geometrical features (i.e., acute corners in low-angle overhang areas) In particular, the selected geometry (shown in

Figure 8) allows one to reproduce a variety of designs in the same part, as the heat exchange conditions are locally varying within the part and in different layers, leading to different hot-spot events in different locations and with different severity.

During actual production scenarios, process parameters are kept fixed, regardless of the shape of the product. Even if optimal process parameters are used for a specific material, hot-spots may occur in the presence of critical geometrical features, because the scanned region is largely surrounded by loose powder; loose powder has a much lower level of heat conductivity than the solid material. The real case study is representative of this kind of critical feature. Finally, during the process, the laser follows different scanning paths in different layers. However, the proposed approach does not depend on the laser scanning path, and hence it can be easily applied to videos captured in different layers, with different geometries and different scan trajectories. In this case study, real hot-spots were observed in different layers and in different locations, which allows us to test the proposed methodology in the presence of different scanning paths and different hot-spot severities.

The same dataset was previously presented in Grasso et al. (2017) and Colosimo and Grasso (2018). The dataset is also publicly available at http://doi.org/10.6084/m9.figshare.7092863.

More details of the experimental setup are discussed in Section 5.1. A performance analysis and a comparison with other benchmark methods are presented in Section 5.2.

# 5.1. Case study setup

The experimental case study previously presented in Grasso et al. (2017) and Colosimo and Grasso (2018) was used to demonstrate the performances of the proposed approach in the presence of real hot-spot events. Previous studies showed that the occurrence of local over-heating conditions may yield geometrical distortions, especially in the presence of thin walls and acute corners. As a consequence of the local heat accumulation, surface tensions of the viscous melt cause the formation of solidified balls on the surface, leading to so-called super-elevated edges (Kleszczynski et al., 2012), i.e., ridges of the solidified material whose height may be higher than the layer thickness. Such local irregularities may propagate and inflate from one layer to another, with possible damage to the powder recoating system. This makes the quick detection of hot-spots particularly relevant in LPBF. As an example, Figure 8 shows the consequence of hot-spots observed during the production of the complex shape used in this real case study in terms of geometrical irregularities in the part.

The same monitoring setup described in Section 4 was applied in this experimentation, but a higher sampling frequency was applied, i.e., f = 300 fps. This sampling frequency was selected as a compromise between the computational feasibility of in-situ image analysis and the ability to capture the process-related dynamic and transitory events without losing relevant information. The spatial resolution was about 150 µm/pixel. An image crop operation was applied to remove defocused regions and areas of the baseplate not involved with the process. The resulting image size was  $121 \times 71$  pixels.

The experimentation consists of an LPBF process on AISI 316L powder with an average particle size of about 25 -30  $\mu$ m for the production of the complex geometry shown Figure (overall dimensions about  $50 \times 50 \times 50$  mm). In this case, three distinct videos were acquired during the LPBF of triangular-shaped slices in three different layers where hot-spots occurred in correspondence to acute corners in over-hang regions. The hotspot events produced local geometrical deformations in the printed part, as highlighted in Figure 8 (right panel). The LPBF process parameters used in the experimentation are summarized in Table 2.

The three video-sequences were labeled as Scenario A, B, and C, respectively. In each scenario, the laser beam passed over the hot-spot region more than once, and hence multiple events were sequentially observed. Different hot-spot events in the same video-sequence refer to the same location, but different time intervals. Each time the laser scanned the defective area in correspondence to acute corners, the heat accumulation produced a hot-spot event that lasted for a few consecutive frames. Figure 9 shows some examples of video frames acquired in the three scenarios. For each scenario, Figure 9 shows one example of video frame under natural melting conditions (top-left panel) and video-frames corresponding to the begin and end of hotspot events that were visible in the video sequence. At least four consecutive hot-spot events in the same location were visible in each scenario.

Figure 10 shows examples of anomalies detected by the proposed method in different scenarios.

#### 5.2. Performance evaluation

Analogous to the simulation study, we applied all the competing methods to Scenarios A, B, and C, and the results are shown in Table 3. We evaluated the capability of competitor methods to detect the four major hot-spot events in each scenario by comparing the time of first signal (expressed in terms of frame index) with the time of first visible hot-spot occurrence in the image stream. When a method was not able to detect the hot-spot event, the symbol "- "is shown in Table 3. Table 3 shows that the proposed method properly detects all the hot-spot events. Following events were detected with no more than five frames of delay, which considerably outperforms all other competing techniques.  $T^2$ , PCA- Lasso- and ST-SSD-based methods were able to detect at most one real hot-spot event. The ST-PCA and Fused

Lasso method were able to detect all the hot-spot events in Scenario A, apart from the very first one, with performances comparable to the ones provided by the proposed approach. However, in Scenario B and Scenario C, the ST-PCA approach allowed signalling only the last (and more severe) hot-spot event, with a larger delay than the proposed method. These results confirm that our proposed spatiotemporal methodology is more effective than the previously proposed ST-PCA technique, and it outperforms more traditional statistical methods for video-imaging analysis.

Table 4 shows the computational time needed by each competing method (all of them were implemented in Matlab® on a standard laptop). The  $T^2$ , PCA, Tucker, and Lasso-based methods were more computationally efficient than the proposed approach, but they provided much less accurate results. The ST-PCA method entails a recursive scheme that inflates the computational cost as new video frames become available. In all the case study analyses, the ST-PCA required less than 0.3 s at each iteration step. Thus, the proposed approach is not only more effective than the ST-PCA for hot-spot detection and localization, but also computationally more efficient. In the present study, all methods were tested in off-line mode, i.e., by first collecting real sensor data during the process and testing the proposed algorithm on these same data after the process. It is worth noting that the computation time of 0.01s required by the proposed approach refers to an implementation on a standard laptop. Because of this, we believe that it is feasible to implement this method for a real-time use exploiting an industrial breadboard implementation that is expected to considerably reduce the computation time.

#### **6 Conclusion**

Online monitoring of high-dimensional spatio-temporal data is gaining increasing interest in not only advanced manufacturing applications but also in non-manufacturing frameworks. In this article we proposed a novel decompositionbased approach for real-time monitoring and anomaly detection of spatio-temporal data. Our method was specifically motivated by the "hot-spot" detection problem in metal AM. The proposed method is able to take advantage of the layer-wise production paradigm to gather as much information as possible about the quality and stability of the process during the process itself, rather than (or in addition to) relying on traditional post-process quality controls. What is missing in industry is the availability of analytical tools able to quickly make sense of gathered data during the process and automatically signal the onset of defects and process instabilities. The proposed method was tested in this framework to demonstrate its ability to overcome the limitation of existing methods. Furthermore, the proposed method is general, and it can be applied to any image-based process monitoring application where the foreground events are random and sparse, and the anomaly is spatially and temporally correlated. To handle the challenges of the high-dimensionality for the video-image stream, we proposed a recursive estimation procedure for real-time implementation of the

algorithm. Finally, a sequential LRT procedure was proposed for online change detection and anomaly localization. To demonstrate the effectiveness of the proposed method, we applied it to both simulated and real data drawn from a real case study in LPBF. Both in the simulation study and in the real case study, the proposed approach outperformed all competitors in terms of RL and anomaly localization accuracy, with a computational cost that was considerably lower than that of its best competitors.

One promising direction for future research consists of extending the proposed method by incorporating a more complex temporal modeling technique for the hot-spot detection, such as a higher-order autoregressive-movingaverage model, to further enhance the characterization of the temporal structure embedded in the spatio-temporal data. Moreover, future studies can be aimed at testing the proposed method in the presence of different kinds of OOC scenarios and different manufacturing applications.

## **Acknowledgments**

The authors would like to thank the Editor, AE and referees for their valuable comments.

## **Funding**

The research of Yan is supported by the NSF grants DMS-1830363 and CMMI-1922739. The research of Paynabar is supported by the NSF grants CMMI-1839591. The research of Prof. B.M. Colosimo and Dr. M. Grasso's research was partially supported by the SIADD Project (Soluzioni Innovative per la qualitá e la sostenibilitá dei processi di ADDitive manufacturing), funded in the framework of the National Operating Programme (PON) "Ricerca e Innovazione 2014-2020".

# **Notes on contributors**

Hao Yan received his BS degree in Physics from the Peking University, Beijing, China, in 2011. He also received a MS degree in Statistics, a MS degree in Computational Science and Engineering, and a PhD degree in Industrial Engineering from Georgia Institute of Technology, Atlanta, in 2015, 2016, 2017, respectively. Currently, he is an Assistant Professor in the School of Computing, Informatics, and Decision Systems Engineering at ASU. His research interests focus on developing scalable statistical learning algorithms for large-scale high-dimensional data with complex heterogeneous structures to extract useful information for the purpose of system performance assessment, anomaly detection, intelligent sampling and decision making. Dr. Yan was also recipients of multiple awards including best paper award in IEEE TASE, IISE Transaction and ASQ Brumbaugh Award. Dr. Yan is a member of INFORMS and IIE.

Marco Grasso is Assistant Professor in the Department of Mechanical Engineering of Politecnico di Milano. He got both his MSc in Aerospace Engineering and his PhD in Mechanical Engineering at Politecnico di Milano. The framework of his research consists of statistical process monitoring of manufacturing processes via signal data analysis, statistical learning and data mining techniques. The core of his research is carried out at the AddMe Lab, the laboratory of the Department of Mechanical Engineering focused on Additive Manufacturing technologies, with a focus on in-situ sensing and monitoring of laser and electron beam powder bed fusion processes.

Kamran Paynabar is the Fouts Family Early Career Professor and Associate Professor in the H. Milton Stewart School of Industrial and Systems Engineering at Georgia Tech. He received his BSc and MSc in Industrial Engineering from Iran, and his PhD in IOE and MA in Statistics from The University of Michigan. His research interests comprise both applied and methodological aspects of machine-learning and statistical modeling integrated with engineering principles. He served as the chair of QSR of INFORMS, and the president of QCRE of IISE. He is an Associate Editor for Technometrics and IEEE-TASE, a Department Editor for IISE-Transactions and a member of the editorial board for Journal of Quality Technology.

Bianca Maria Colosimo is Professor in the Department of Mechanical Engineering of Politecnico di Milano, where she is Deputy-Head of the Department. She received her MSc and PhD (cum Laude) in Industrial Engineering from Politecnico di Milano. Her research interest is mainly in the area of complex data modeling monitoring and control, with special attention to surface point clouds, signal, images and video data in advanced manufacturing applications, additive manufacturing among the others. She is Editor-in-Chief of the Journal of Quality Technology, member of the QSR Advisory Board at INFORMS, Council member of ENBIS, member of the Implementation Support Group of the Manufuture-EU, member of the CLC South of the European Institute of Innovation & Technology (EIT) on Manufacturing. She is included among the top 100 Italian woman scientists in STEM - (https://100esperte.it/search?id=170).

#### **ORCID**

Hao Yan http://orcid.org/0000-0002-4322-7323 Marco Grasso (D) http://orcid.org/0000-0003-3233-4198

#### References

Celik, T. (2009) Unsupervised change detection in satellite images using principal component analysis and k-means clustering. IEEE Geoscience and Remote Sensing Letters, 6(4), 772-776.

Cheng, K.W., Chen, Y.T. and Fang, W.H. (2015) Video anomaly detection and localization using hierarchical feature representation and Gaussian process regression, in Proceedings of the IEEE Conference on Computer Vision and Pattern Recognition, IEEE Press, Piscataway, NJ, pp. 2909-2917.

Colosimo, B.-M. and Grasso, M. (2018) Spatially weighted PCA for monitoring video image data with application to additive manufacturing. Journal of Quality Technology, 50(4), 391-417.

Everton, S.-K., Hirsch, M., Stravroulakis, P., Leach, R.-K. and Clare, A.-T. (2016) Review of in-situ process monitoring and in-situ metrology for metal additive manufacturing. Materials and Design, **95**, 431-445.

Gertler, J. (2017) Fault Detection and Diagnosis in Engineering Systems, CRC Press, Boca Raton, FL.

Glaz, J., Naus, J.I., Wallenstein, S., Wallenstein, S. and Naus, J.I. (2001) Scan Statistics, Springer, New York, NY.

Gobert, C., Reutzel, E.W., Petrich, J., Nassar, A.R. and Phoha, S. (2018) Application of supervised machine learning for defect detection during metallic powder bed fusion additive manufacturing using high resolution imaging. Additive Manufacturing, 21, 517-528.

Grasso, M. and Colosimo, B.M. (2017) Process defects and in situ monitoring methods in metal powder bed fusion: A review. Measurement Science and Technology, 28(4), 044005.

Grasso, M., Laguzza, V., Semeraro, Q. and Colosimo, B.M. (2017) Inprocess monitoring of selective laser melting: Spatial detection of defects via image data analysis. Journal of Manufacturing Science and Engineering, 139(5), 051001.

Hotelling, H. (1992) The generalization of student's ratio, in Breakthroughs in Statistics, Springer, New York, NY, pp. 54-65.

Jolliffe, I. (2002) Principal Component Analysis, Wiley Online Library,

Khairallah, S.A., Anderson, A.T., Rubenchik, A. and King, W.E. (2016) Laser powder-bed fusion additive manufacturing: Physics of complex melt flow and formation mechanisms of pores, spatter, and denudation zones. Acta Materialia, 108, 36-45.

- Kleszczynski, S., Zur Jacobsmühlen, J., Sehrt, J. and Witt, G. (2012) Error detection in laser beam melting systems by high resolution imaging, in Proceedings of the Solid Freeform Fabrication Symposium, University of Texas, pp. 975-987.
- Kwon, O., Kim, H.G., Ham, M.J., Kim, W., Kim, G.H., Cho, J.H., Kim, N.I. and Kim, K. (2020) A deep neural network for classification of melt-pool images in metal additive manufacturing. Journal of Intelligent Manufacturing, 31(2), 375-386.
- Li, W., Mahadevan, V. and Vasconcelos, N. (2014). Anomaly detection and localization in crowded scenes. IEEE Transactions on Pattern Analysis and Machine Intelligence, 36(1), 18-32.
- Liu, J., Yuan, L., and Ye, J. (2010) An efficient algorithm for a class of fused lasso problems, in Proceedings of the 16th ACM SIGKDD International Conference on Knowledge Discovery and Data Mining, Elsevier, pp. 323-332.
- Liu, Y., Yang, Y., Mai, S., Wang, D. and Song, C. (2015) Investigation into spatter behavior during selective laser melting of AISI 316L stainless steel powder. Materials and Design, 87, 797-806.
- Lu, C.W. and Reynolds Jr, M.R. (1999) EWMA control charts for monitoring the mean of autocorrelated processes. Journal of Quality Technology, 31(2), 166-188.
- Megahed, F.M., and Jones Farmer, L.A. (2015) Statistical perspectives on "big data", in Frontiers in Statistical Quality Control 11, Springer, New York, NY, pp. 29-47.
- Megahed, F.M., Woodall, W.H. and Camelio, J.A. (2011) A review and perspective on control charting with image data. Journal of Quality Technology, 43(2), 83-98.
- Mood, A.M. (1950) Introduction to the Theory of Statistics, McGraw Hill, New York, NY.
- Neil, J., Hash, C., Brugh, A., Fisk, M. and Storlie, C.B.J.T. (2013) Scan statistics for the online detection of locally anomalous subgraphs. Technometrics, 55(4), 403-414.
- Nomikos, P. and MacGregor, J.F. (1995) Multivariate SPC charts for monitoring batch processes. Technometrics, 37(1), 41-59.
- Oakland, R.J. and Oakland, J.S. (2007) Statistical Process Control, Routledge, New York, NY.
- Okaro, I.A., Jayasinghe, S., Sutcliffe, C., Black, K., Paoletti, P. and Green, P.L. (2019) Automatic fault detection for laser powder-bed fusion using semi-supervised machine learning. *Manufacturing*, **27**, 42–53.
- Paynabar, K., Jin, J. and Pacella, M. (2013) Monitoring and diagnosis of multichannel nonlinear profile variations using uncorrelated multilinear principal component analysis. IIE Transactions, 45(11), 1235-1247.
- Paynabar, K., Zou, C. and Qiu, P. (2016) A change-point approach for Phase-I analysis in multivariate profile monitoring and diagnosis. Technometrics, 58(2), 191-204.

- Powers, D.M. (2020) Evaluation: From precision, recall and F-measure to ROC, informedness, markedness and correlation. arXiv preprint arXiv:2010.16061.
- Qiu, P., Zou, C. and Wang, Z. (2010) Nonparametric profile monitoring by mixed effects modeling. Technometrics, 52(3), 265-277.
- Rijsbergen, C.J. (1979) Information Retrieval, Butterworths, London.
- Scime, L. and Beuth, J. (2018) Anomaly detection and classification in a laser powder bed additive manufacturing process using a trained computer vision algorithm. Additive Manufacturing, 19, 114-126.
- Sergin, N. and Yan, H. (2019) High-dimensional nonlinear profile monitoring based on deep probabilistic autoencoders. arXiv preprint arXiv:1911.00482.
- Stucker, B., Gibson, I. and Rosen, D. (2010) Additive Manufacturing Technologies. Springer, New York, NY.
- Tibshirani, R. (1996) Regression shrinkage and selection via the lasso. Journal of the Royal Statistical Society. Series B (Methodological), 58(1), 267-288.
- Tsutsumida, N., Harris, P. and Comber, A. (2017) The application of a geographically weighted principal components analysis for exploring 23 years of goat population change across Mongolia. Annals of the American Association of Geographers, 107(5), 1060-1074.
- Xin, B., Kawahara, Y., Wang, Y. and Gao, W. (2014) Efficient generalized fused lasso and its application to the dagnosis of Alzheimer's disease, in Proceedings of the AAAI Conference on Artificial Intelligence, AAAI Press, pp. 2163-2169.
- Yan, H., Paynabar, K. and Shi, J. (2015) Image-based process monitoring using low-rank tensor decomposition. IEEE Transactions on Automation Science and Engineering, 12(1), 216-227.
- Yan, H., Paynabar, K. and Shi, J. (2017) Anomaly detection in images with smooth background via smooth-sparse decomposition. Technometrics, **59**(1), 102–114.
- Yan, H., Paynabar, K. and Shi, J. (2018) Real-time monitoring of highdimensional functional data streams via spatio-temporal smooth sparse decomposition. Technometrics, 60(2), 181-197.
- Zhang, C., Yan, H., Lee, S. and Shi, J. (2018) Weakly correlated profile monitoring based on sparse multi-channel functional principal component analysis. IISE Transactions, 50(10), 878-891.
- Zhang, C., Yan, H., Lee, S. and Shi, J. (2020) Dynamic multivariate functional data modeling via sparse subspace Technometrics, in press.
- Zou, C. and Qiu, P. (2009) Multivariate statistical process control using lasso. Journal of the American Statistical Association, 104(488), 1586-1596.
- Zou, C., Qiu, P. and Hawkins, D. (2009) Nonparametric control chart for monitoring profiles using change point formulation and adaptive smoothing. Statistica Sinica, 19(3), 1337–1357.
- Zou, C., Tsung, F., and Wang, Z. (2008) Monitoring profiles based on nonparametric regression methods. Technometrics, 50(4), 512-526.